



Title	DME Dissociation Reaction on Platinum Electrode Surface : A Quantitative Kinetic Analysis by In Situ IR Spectroscopy
Author(s)	Zhang, Yi; Tong, Yujin; Lu, Leilei; Osawa, Masatoshi; Ye, Shen
Citation	Journal of The Electrochemical Society, 157(1), F10-F15 <a href="https://doi.org/10.1149/1.3243847">https://doi.org/10.1149/1.3243847</a>
Issue Date	2010
Doc URL	<a href="http://hdl.handle.net/2115/42505">http://hdl.handle.net/2115/42505</a>
Rights	© The Electrochemical Society, Inc. 2010. All rights reserved. Except as provided under U.S. copyright law, this work may not be reproduced, resold, distributed, or modified without the express permission of The Electrochemical Society (ECS). The archival version of this work was published in J. Electrochem. Soc., Volume 157, Issue 1, pp. F10-F15 (2010).
Type	article
File Information	JES000F10.pdf



[Instructions for use](#)



## DME Dissociation Reaction on Platinum Electrode Surface: A Quantitative Kinetic Analysis by In Situ IR Spectroscopy

Yi Zhang,<sup>a</sup> Yujin Tong,<sup>a</sup> Leilei Lu,<sup>a</sup> Masatoshi Osawa,<sup>a,\*</sup> and Shen Ye<sup>a,b,z</sup>

<sup>a</sup>Catalysis Research Center, Hokkaido University, Sapporo, 001-0021, Japan

<sup>b</sup>Precursory Research for Embryonic Science and Technology (PRESTO), Japan Science and Technology Agency (JST), Kawaguchi 332-0012, Japan

The kinetics of electrocatalytic dissociation reaction of dimethyl ether (DME) on a platinum (Pt) polycrystalline electrode in an acidic solution yielding carbon monoxide (CO) has been quantitatively analyzed by in situ IR spectroscopy in the potential region between 100 and 500 mV (vs reversible hydrogen electrode). A two-step consecutive reaction model, an initial dehydrogenation step followed by a CO formation step, is proposed for the dissociation process of the DME molecule. The mechanism of the DME dissociation on the Pt electrode surface is discussed based on the kinetic analysis.

© 2009 The Electrochemical Society. [DOI: 10.1149/1.3243847] All rights reserved.

Manuscript submitted April 22, 2009; revised manuscript received September 4, 2009. Published November 3, 2009.

Dimethyl ether (DME, CH<sub>3</sub>OCH<sub>3</sub>) is considered a promising fuel in direct fuel cells<sup>1-6</sup> because of several advantages over methanol and other small organic molecules: higher energy density, lower toxicity, and lower crossover to the cathode.<sup>1,2</sup> Several studies on direct dimethyl ether fuel cell (DDFC) aiming for a high performance have been carried out.<sup>1-6</sup> However, the output of DDFC is still lower than that of direct methanol fuel cell. Further understanding and control of the kinetics and mechanism of the DME anodic reaction on electrocatalyst surfaces, especially in the low overpotential region where the fuel cell is commonly operated, is crucial to develop highly efficient catalysts for DDFC.

Recently, we investigated the electro-oxidation of DME molecules on Pt single-crystalline and polycrystalline electrode surfaces using electrochemistry and in situ IR spectroscopy.<sup>7-9</sup> Several reaction intermediates have been confirmed before bulk oxidation of DME occurs. An intermediate assigned to (CH<sub>3</sub>OCH<sub>2</sub>)<sub>ad</sub> is formed in a dehydrogenation reaction and successively oxidized to CO<sub>ad</sub> in the potential region between 100 and 500 mV where the DME dissociation reaction takes place. The C-H activation process has been proposed as the initial step for the electro-oxidation of small organic molecules on Pt electrode surfaces.<sup>10,11</sup> Waszczuk et al.<sup>12-14</sup> proposed that the C-H bond split of methanol to yield -CH<sub>2</sub>OH is an elementary step for its oxidative dissociation on Pt(111) and Pt(110) electrode surfaces from voltammetric and chronoamperometric measurements. However, it is difficult to make further comprehensive analysis on kinetics and mechanisms only from these electrochemical measurements because two or more reactions can occur simultaneously or successively and the currents observed probably arise from different reaction steps. In situ IR spectroscopy can provide structural information on reaction intermediates and products on the electrode surface during electrochemical reactions. IR spectroscopy is expected to be employed to study the reaction kinetics of different intermediates on the electrode surface owing to its chemical specificity, while the successful examples are still limited due to the short lifetime of these intermediates in comparison with the time resolution of the Fourier transform infrared (FTIR) measurement.

In the present study, surface-enhanced IR spectroscopy with the Kretschmann attenuated total reflection (ATR) configuration<sup>15-19</sup> is employed to investigate the kinetics of the dissociation process of DME molecules on the Pt polycrystalline electrode surface in an acidic solution. A quantitative analysis on the kinetics behaviors of the dissociation intermediates, (CH<sub>3</sub>OCH<sub>2</sub>)<sub>ad</sub> and CO<sub>ad</sub>, is utilized to discuss the possible reaction mechanism of DME on the Pt electrode surface.

### Experimental

The details of the in situ surface-enhanced IR measurements with the Kretschmann ATR configuration for DME electro-oxidation were described in Ref. 7. A Pt thin film served as the working electrode. It was chemically deposited on the flat surface of a hemicylindrical Si prism.<sup>17,20</sup> Briefly, the Si surface was activated first by contacting with 0.5% HF containing 1 mM PdCl<sub>2</sub>, which can improve the adhesion of the deposited metal film to the Si substrate. Then, Pt was chemically deposited to form a 50 nm thick film with a commercially available plating solution (LECTROLESS PT100, Electroplating Engineering of Japan) at 60°C.

The electrode potential was controlled by a potentiostat (EG&G PARC model 263A). All potentials in the paper are presented with respect to the reversible hydrogen electrode (RHE). The IR measurements were carried out using a BioRad FTIR-575C spectrometer equipped with a mercury-cadmium-telluride detector. The IR spectra were recorded in the fast scan mode with a spectral resolution of 4 cm<sup>-1</sup>. Five interferograms were coadded to each spectrum, which required 1 s to get one spectrum. A potential program shown in Scheme 1 is employed for the present time-resolved IR measurements. The potential was set at 1500 mV for 2 s to remove any possible organic adsorbates and turned back to 50 mV for 2 s to reduce oxide on the electrode surface. Finally, the potential was stepped to a target potential,  $E_{ad}$  (50–500 mV), for 300 s, where the time-resolved IR spectra were recorded. All IR spectra were shown in absorbance units referenced to a background spectrum recorded at 50 mV in the electrolyte solution before DME introduction.

A flow cell was employed for in situ IR measurements to remove a possible influence from the accumulation of reaction intermediates and products dissolved in the electrolyte. The solution in the flow cell can be replaced by a fresh electrolyte solution more than five times per minute.<sup>7</sup> The supporting electrolyte solutions were prepared from Milli-Q water (>18 MΩ) and analytical grade HClO<sub>4</sub> and were deaerated with Ar for 30 min before use. After electrochemically cleaning the electrode surface by successive potential cycles between 50 and 1500 mV in the blank electrolyte, a reference spectrum was recorded at 50 mV. Then, the solution was saturated with DME (ca. 1.65 M)<sup>9</sup> by bubbling DME (99.99%, Sumitomo Chemicals Corp.) through the solution. All experiments were carried out at room temperature (22°C).

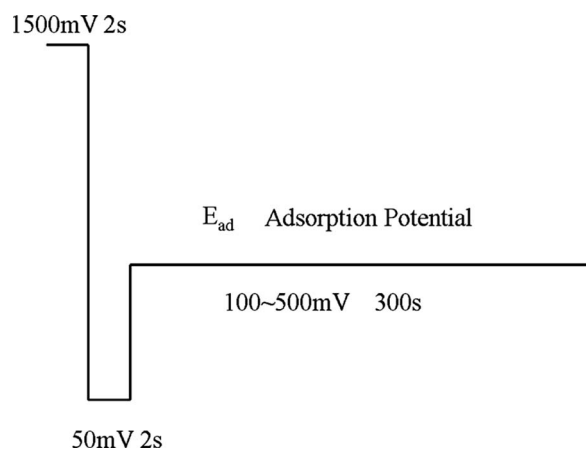
A nonlinear least-squares fitting program, the Levenberg-Marquardt algorithm provided by Origin 7.0 (OriginLab), was used to analyze the time profile of IR band intensities.

### Results and Discussion

*Time-resolved IR measurement on DME dissociation reaction.*—As the Pt electrode surface is fully covered by a full monolayer of adsorbed hydrogen (H<sub>ad</sub>), for example, at 50 mV, no

\* Electrochemical Society Active Member.

<sup>z</sup> E-mail: ye@cat.hokudai.ac.jp



**Scheme 1.** The potential scheme for the time-resolved IR measurement where  $50 \text{ mV} < E_{\text{ad}} < 500 \text{ mV}$ .

dissociation of DME was observed by both electrochemical and in situ IR measurements (results are not shown), indicating that  $\text{H}_{\text{ad}}$  retards the DME reaction on the Pt electrode surface. After stepping to a potential ( $E_{\text{ad}}$ ) higher than 50 mV (Scheme 1), a part or all of  $\text{H}_{\text{ad}}$  are desorbed from the Pt surface depending on  $E_{\text{ad}}$ , and several reaction intermediates are observed.<sup>7</sup> It is expected that DME can react with the Pt electrode surface sites free from  $\text{H}_{\text{ad}}$ .

Figure 1a shows a set of time-resolved IR spectra after stepping the potential to 300 mV. Several IR bands appear at around 1322, 1445, and 1480  $\text{cm}^{-1}$  immediately after the potential step. The intensities of these IR bands reach maxima in 15 s and then gradually decrease to zero after ca. 200 s. The peak positions of these IR bands slightly shift after the potential step. For example, the IR band at 1322  $\text{cm}^{-1}$  blueshifts to 1326  $\text{cm}^{-1}$  as its band intensity reaches maximum and then gradually redshifts to a lower frequency with a decrease in band intensity. The shifts for the band position suggest that these IR bands are contributed from adsorbed species.<sup>7</sup> To simplify the description in the following text, the positions for these peaks were denoted as they first appeared. Slightly later than the appearance of the three peaks, an IR band appears at around 1995  $\text{cm}^{-1}$  (Fig. 1a). The peak intensity increases and the peak position blueshifts with time. The stable peak is observed at 2050  $\text{cm}^{-1}$  after 200 s. Another broad IR band is observed at around 1810  $\text{cm}^{-1}$  after ca. 50 s. The peak position also shifts to a higher frequency with time accompanied by an increase in peak intensity. The intensities of these two peaks reach saturation after ca. 200 s.

Similar features are also observed at 400 mV but with different time profiles, as shown in Fig. 1b. In comparison to the results obtained at 300 mV, the intensities of the IR bands at 1322, 1445, and 1480  $\text{cm}^{-1}$  reach their maxima in a shorter time (5 s) and then rapidly decrease to zero after ca. 50 s. The two IR bands observed in the frequency region between 1800 and 2100  $\text{cm}^{-1}$  show higher

intensities and frequencies than those observed at 300 mV at the same reaction time and reach saturation after ca. 100 s.

As already discussed in our previous paper,<sup>7</sup> the bands at 1480, 1455, and 1322  $\text{cm}^{-1}$  can be assigned to the  $\text{CH}_3$  ( $\delta_{\text{CH}}$ ) and  $\text{CH}_2$  ( $\delta_{\text{CH}}$ ) deformation modes and the  $\text{CH}_2$  wagging  $\omega(\text{CH}_2)$  mode, respectively, of an intermediate species  $(\text{CH}_3\text{OCH}_2^-)_{\text{ad}}$  adsorbed on the Pt electrode surface. Two IR bands at around 2050 and 1850  $\text{cm}^{-1}$  are assigned to the C–O stretching mode of linearly bonded carbon monoxide ( $\text{CO}$ ) ( $\text{CO}_{\text{L}}$ ) and bridge-bonded  $\text{CO}$  ( $\text{CO}_{\text{B}}$ ). Both  $(\text{CH}_3\text{OCH}_2^-)_{\text{ad}}$  and  $\text{CO}_{\text{ad}}$  were formed from the DME dissociation process in the potential region more negative than 600 mV. Peaks related to  $(\text{CH}_3\text{OCH}_2^-)_{\text{ad}}$  always appear earlier than  $\text{CO}$  adsorbed species and then disappear with the appearance of the  $\text{CO}$  peak.<sup>7</sup>

Figure 2 summarizes the integrated IR band intensities for  $(\text{CH}_3\text{OCH}_2^-)_{\text{ad}}$  at 1322  $\text{cm}^{-1}$  (circles) and 1480  $\text{cm}^{-1}$  (triangles) and  $\text{CO}_{\text{L}}$  at 2050  $\text{cm}^{-1}$  (squares) as a function of time after the potential is stepped from 50 mV to (a) 100, (b) 150, (c) 200, (d) 250, (e) 300, (f) 350, (g) 400, (h) 450, and (i) 500 mV. The band intensities for  $(\text{CH}_3\text{OCH}_2^-)_{\text{ad}}$  are multiplied by a factor of 5 for comparison with that of  $\text{CO}_{\text{L}}$ . The time profiles demonstrate that the two reaction intermediates were formed in a successive way; i.e.,  $(\text{CH}_3\text{OCH}_2^-)_{\text{ad}}$  is generated first from DME and then further decomposed to  $\text{CO}_{\text{ad}}$ . The time profiles apparently depend on the electrode potential. At higher potentials, the formation of  $(\text{CH}_3\text{OCH}_2^-)_{\text{ad}}$  and  $\text{CO}_{\text{L}}$  takes place in a shorter period.

Because the coverage of species adsorbed on the electrode surface is proportional to its IR band intensity, the time-resolved IR results observed above (Fig. 2) can be used as a quantitative analysis on the kinetics of DME dissociation at different  $E_{\text{ad}}$ .

*Quantitative analysis by a consecutive reaction model.*— As described above, after the potential is stepped to  $E_{\text{ad}}$  higher than 50 mV, it is assumed that DME molecules occupy  $\text{H}_{\text{ad}}$ -free Pt sites as physically adsorbed forms of  $(\text{CH}_3\text{OCH}_3)_{\text{ad}}$  and further decompose into  $(\text{CH}_3\text{OCH}_2^-)_{\text{ad}}$  and  $\text{CO}_{\text{ad}}$  in a successive way, as shown in the following scheme<sup>21</sup>



or in a simplified form



where R, I, and P represent reactant  $(\text{CH}_3\text{OCH}_3)_{\text{ad}}$ , intermediate  $(\text{CH}_3\text{OCH}_2^-)_{\text{ad}}$ , and product  $\text{CO}_{\text{ad}}$ , respectively. As a first approximation, these elementary steps are assumed to be first-order reaction.  $k_a$  and  $k_b$  represent the rate constants for dehydrogenation and  $\text{CO}$  formation steps, respectively. The backward reaction rates are assumed to be very low and are ignored in the work. In the present kinetics analysis model, it is assumed that R, I, and P species occupy the identical surface sites during the reaction process.

Under these assumptions, the reaction rates for R, I, and P in Eq. 1b can be expressed by the following differential equations

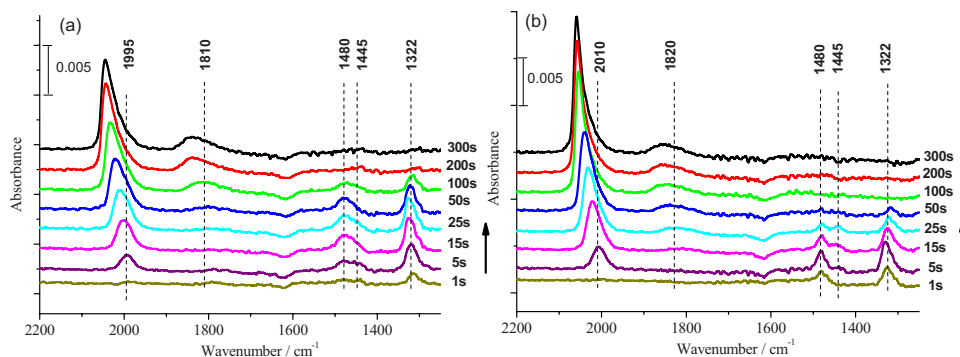


**Figure 1.** (Color online) The in situ IR spectra recorded during the DME dissociation process on a polycrystalline Pt electrode at (a) 300 and (b) 400 mV.

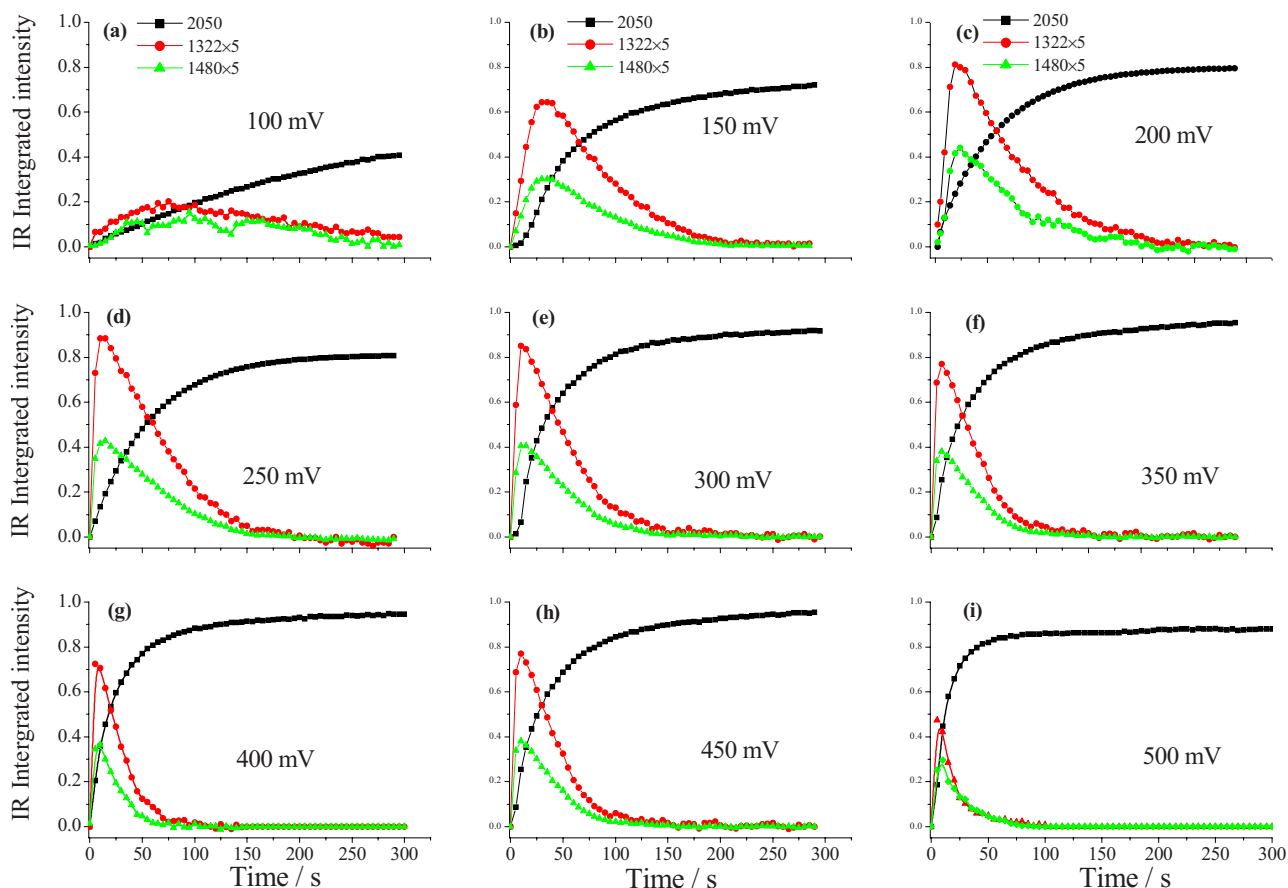


**Figure 2.** (Color online) The integrated IR intensities for bands at 2050  $\text{cm}^{-1}$  (squares), 1322  $\text{cm}^{-1}$  (circles), and 1480  $\text{cm}^{-1}$  (triangles) during the DME dissociation process at (a) 100, (b) 150, (c) 200, (d) 250, (e) 300, (f) 350, (g) 400, (h) 450, and (i) 500 mV for the first 300 s after the potential step from 50 mV. The IR band intensities at 1322 and 1480  $\text{cm}^{-1}$  are multiplied by a factor of 5.

$$\frac{d\theta_R(t)}{dt} = -k_a\theta_R(t) \quad [2a]$$

$$\frac{d\theta_I(t)}{dt} = k_a\theta_R(t) - k_b\theta_I(t) \quad [2b]$$

$$\frac{d\theta_P(t)}{dt} = k_b\theta_I(t) \quad [2c]$$

where  $\theta_x(t)$  ( $x = R, I,$  and  $P$ ) represent the surface coverage of each species at time  $t$ .  $\theta_x(t)$ ,  $k_a$ , and  $k_b$  are also dependent on potential. As the potential is stepped to  $E_{ad}$  at  $t = 0$ ,  $\theta_I(0) = \theta_P(0) = 0$ , DME starts to dissociate to  $(\text{CH}_3\text{OCH}_2^-)_{ad}$  and further to  $\text{CO}_{ad}$  in a step-wise way. At a prolonged reaction time (i.e.,  $t \rightarrow \infty$ ),  $(\text{CH}_3\text{OCH}_3)_{ad}$  and  $(\text{CH}_3\text{OCH}_2^-)_{ad}$  are fully converted into a stable product of  $\text{CO}_{ad}$ . That is

$$\theta_R(\infty) = \theta_I(\infty) = 0, \quad \theta_P(\infty) = \theta_R(0) = \theta_{\text{CO}}(\infty)$$

$$\theta_R(t) + \theta_I(t) + \theta_P(t) = \theta_{\text{total}}$$

where  $\theta_{\text{total}}$  represents the total surface coverage at the potential  $E_{ad}$ , which is assumed to be equal to the initial  $\theta_R(0)$  here.

Based on these boundary conditions, the solutions for the above differential equations Eq. 2a-2c can be obtained as<sup>21</sup>

$$\theta_R(t) = \theta_{\text{total}}e^{-k_a t} \quad [3a]$$

$$\theta_I(t) = \frac{k_a}{k_b - k_a} (e^{-k_a t} - e^{-k_b t}) \theta_{\text{total}} \quad [3b]$$

$$\theta_P(t) = \left( 1 + \frac{k_a e^{-k_b t} - k_b e^{-k_a t}}{k_b - k_a} \right) \theta_{\text{total}} \quad [3c]$$

As described above, the coverage for I and P can be estimated from the intensities of  $(\text{CH}_3\text{OCH}_2^-)_{ad}$  and  $\text{CO}_{ad}$  bands observed in the time-resolved IR spectra. Assuming the IR band intensity for species  $x$  adsorbed on the electrode surface at time  $t$ ,  $A_x(t)$ , being proportional to its coverage  $\theta_x$

$$A_I(t) = \alpha_I \times \theta_I(t) \quad [4a]$$

$$A_P(t) = \alpha_P \times \theta_P(t) \quad [4b]$$

where  $\alpha_I$  and  $\alpha_P$  represent IR absorption coefficients for species I and P, respectively. From Eq. 4a and 4b

$$\frac{A_I(t)}{A_P(t)} = \frac{\alpha_I}{\alpha_P} \times \frac{\theta_I(t)}{\theta_P(t)} = N \times \frac{\theta_I(t)}{\theta_P(t)} \quad [5]$$

Here,  $N$  is the ratio of the IR absorption coefficient for the vibrational modes of I and P and is used as the correction factor in the present work to directly compare the IR band intensities for  $(\text{CH}_3\text{OCH}_2^-)_{ad}$  and  $\text{CO}_{ad}$  species. It is assumed that  $\alpha_I$  and  $\alpha_P$  are independent of electrode potential and coverage; i.e.,  $N$  is regarded as a constant in the potential region. Both IR bands at 1322  $\text{cm}^{-1}$  [ $\omega(\text{CH}_2)$ ] and 1480  $\text{cm}^{-1}$  ( $\delta_{\text{CH}}$ ) can be used to stand the coverage of  $(\text{CH}_3\text{OCH}_2^-)_{ad}$  in the following kinetic analysis (of course,  $N$  values are different due to the different IR absorption coefficients). The analysis is valid only if the results obtained independently from the two IR bands are identical. The IR dipole moment of  $\text{CO}_L$  is

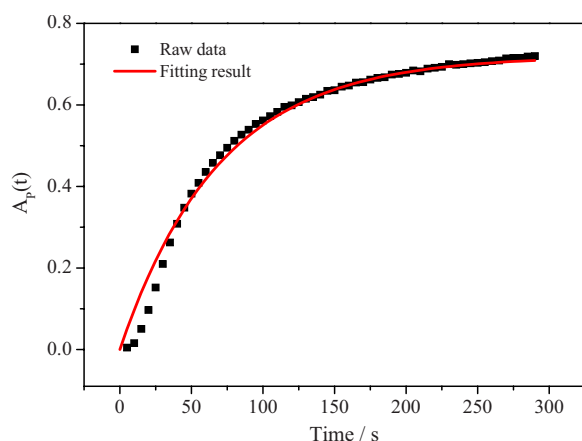


**Figure 3.** (Color online) IR raw data for  $\text{CO}_L$  (squares) and the fitting result (solid line) at 150 mV by Eq. 7. See text for details.

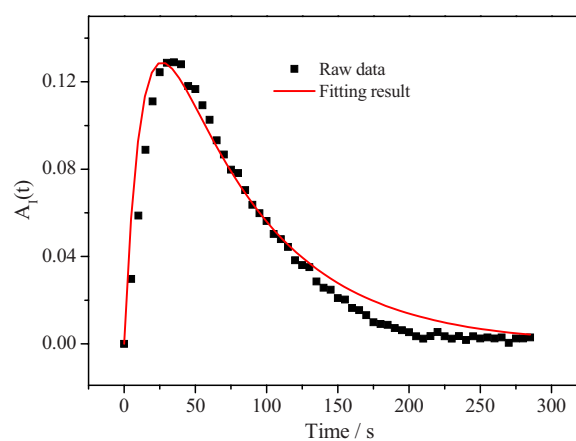


**Figure 4.** (Color online) IR raw data for  $(\text{CH}_3\text{OCH}_2^-)_{\text{ad}}$  (squares) and the fitting result (solid line) at 150 mV by Eq. 6a. See text for details.

much larger than most of the other vibrational modes;<sup>22,23</sup> therefore, we have  $0 < N \ll 1$  for Eq. 5.

As shown in Fig. 2, most of the IR band intensities obtained at various potentials reach a saturation at 300 s except that at 100 mV (IR results obtained at potentials lower than 150 mV were not quantitatively analyzed by the kinetics model because they did not satisfy the boundary conditions).  $A_x^{(t)}$  at 300 s is roughly assumed to be an IR intensity at a steady state ( $t \rightarrow \infty$ ) for species  $x$ . The  $\text{CO}_L$  band is used here to represent all of the  $\text{CO}_{\text{ad}}$  as the first approximation. Assuming that the reaction reaches a steady state at a certain potential  $E_{\text{ad}}$ ,  $\theta_{\text{total}}$  can be described by  $A_P(\infty)$

$$\theta_{\text{total}} = \theta_P(\infty) \approx \theta_{\text{CO}_L}(\infty) = \alpha_P \times A_P(\infty)$$

From Eq. 3b, 3c, and 5, we have

$$A_1(t) = N \frac{k_a}{k_b - k_a} (e^{-k_a t} - e^{-k_b t}) \times A_P(\infty) \quad [6a]$$

$$A_P(t) = \left( 1 + \frac{k_a e^{-k_b t} - k_b e^{-k_a t}}{k_b - k_a} \right) \times A_P(\infty) \quad [6b]$$

Three unknown factors,  $N$ ,  $k_a$ , and  $k_b$ , are included in Eq. 6. Equation 6b can be further simplified under certain boundary conditions. From the electrochemical and IR observations (Fig. 2), it is empirically known that the rate of the CO formation step ( $k_b$ ) is rather slow in comparison to that of the dehydrogenation steps ( $k_a$ ) in the potential region less positive than 200 mV. Under such condition, i.e.,  $k_a \gg k_b$ , Eq. 6b can be simplified to

$$A_P(t) \approx (1 - e^{-k_b t}) \times A_P(\infty) \quad [7]$$

Thus,  $k_b$  can be determined by fitting the time profile of IR intensity for  $\text{CO}_{\text{ad}}$  observed in the low potential region based on Eq. 7, using a nonlinear least-squares fitting program with the Levenberg–Marquardt algorithm. Figure 3 shows raw data (squares) and fitting result (solid trace) at 150 mV. Except for the small deviation within the initial 20 s, the fitting curve can quantitatively reproduce the time profile of the observed  $\text{CO}_{\text{ad}}$  band intensity.  $k_b$  is determined to be  $0.014 \text{ s}^{-1}$  from the fitting. Then, the value of  $k_b$  is substituted into Eq. 6a, and the other two parameters,  $k_a$  and  $N$ , are determined as  $0.11 \text{ s}^{-1}$  and 0.26, respectively, by fitting the time profile of the IR band at  $1322 \text{ cm}^{-1}$  for  $(\text{CH}_3\text{OCH}_2^-)_{\text{ad}}$  at the same potential (Fig. 4).

The fitting results show that  $k_a$  ( $0.11 \text{ s}^{-1}$ ) is much larger than that of  $k_b$  ( $0.014 \text{ s}^{-1}$ ) at this potential (150 mV), and this agrees with our previous assumption. Because  $k_a$  and  $k_b$  are mathematically exchangeable (Eq. 6b), if one assumes  $k_a \ll k_b$ , we can get another set of solutions from the fitting process where  $k_a = 0.014 \text{ s}^{-1}$ ,  $k_b$

$= 0.062 \text{ s}^{-1}$ , and  $N = 1.2$ . However, this solution is not true because  $N$  is higher than 1 in that case and is contradictory to our initial condition for the correction factor  $N$  ( $0 < N \ll 1$ ).

The same fitting processes have also been carried out for the IR results at 200 mV (Fig. 2c), and the value of  $N$  is determined as 0.28 from the IR band at  $1322 \text{ cm}^{-1}$  and is comparable to that determined at 150 mV ( $N = 0.26$ ), which confirms that the present fitting procedures are reasonable. The  $N$  of 0.26 was used in the following fitting process on the other potentials.

The approximation in Eq. 7 was only used one time at the low potential region (where  $k_a \gg k_b$ ) to determine  $k_b$  and then to further determine  $k_a$  and  $N$  with Eq. 6a at the same potential. Because  $N$  is a constant and is independent of the potential, the  $N$  determined here was used as a constant to determine  $k_a$  and  $k_b$  at a potential between 150 and 500 mV by fitting the time profiles of the IR intensity for  $(\text{CH}_3\text{OCH}_2^-)_{\text{ad}}$  using Eq. 6a without further approximation assumption.  $A_P(t \rightarrow \infty)$  can be directly obtained from the time profile of the IR intensity for  $(\text{CO})_{\text{ad}}$  at  $t = 300 \text{ s}$  at each potential. Figure 5 shows fitting results at 300 and 400 mV, respectively.  $k_a$  and  $k_b$  are determined to be 0.155 and  $0.023 \text{ s}^{-1}$  at 300 mV and 0.21 and  $0.052 \text{ s}^{-1}$  at 400 mV, respectively.

Table I summarizes the rate constants of  $k_a$  and  $k_b$  based on fitting the time profiles of IR bands at  $1320$  and  $2050 \text{ cm}^{-1}$ .  $k_a$  increases from  $0.112 \pm 0.02 \text{ s}^{-1}$  at 150 mV to  $0.209 \pm 0.03 \text{ s}^{-1}$  at 400 mV and then decreases to  $0.082 \pm 0.015 \text{ s}^{-1}$  at 500 mV, while  $k_b$  increases from  $0.014 \pm 0.002 \text{ s}^{-1}$  at 150 mV to  $0.136 \pm 0.01 \text{ s}^{-1}$  at 500 mV. In the potential region between 100 and 450 mV,  $k_a$  is always larger than  $k_b$ .

Similar fitting procedures have also been carried out using the IR band profiles at  $1480 \text{ cm}^{-1}$  for  $(\text{CH}_3\text{OCH}_2^-)_{\text{ad}}$  and  $2050 \text{ cm}^{-1}$  for  $\text{CO}_L$ . In this case,  $N$  was determined to be 0.12. The lower  $N$  value comes from the smaller IR absorption coefficient for the band at  $1480 \text{ cm}^{-1}$  than that at  $1322 \text{ cm}^{-1}$ . Table II summarizes these fitting parameters for  $k_a$  and  $k_b$  from the IR bands at 1480 and  $2050 \text{ cm}^{-1}$ . The values of  $k_a$  and  $k_b$  in Table II are fairly close to those in Table I, indicating that the present analysis procedure is reasonable because the bands at 1480 and  $1322 \text{ cm}^{-1}$  represent the same species  $(\text{CH}_3\text{OCH}_2^-)_{\text{ad}}$ .

Figure 6 shows the relationship between the potential and the logarithm of rate constants of  $k_a$  (solid symbols) and  $k_b$  (open symbols), i.e., the Tafel plot, determined by the above kinetics analyses. To show the validity of the fitting process,  $k_a$  and  $k_b$  were calculated from the band at  $1320 \text{ cm}^{-1}$  (squares) and  $1480 \text{ cm}^{-1}$  (triangles). As shown in Fig. 6,  $k_a$  increases slowly with potential. At a potential higher than 400 mV,  $k_a$  starts to decrease. A linear relation is observed in the potential region between 150 and 450 mV with a large slope (i.e., Tafel slope) of ca.  $1200 \pm 100 \text{ mV/dec}$ .  $k_b$  is smaller

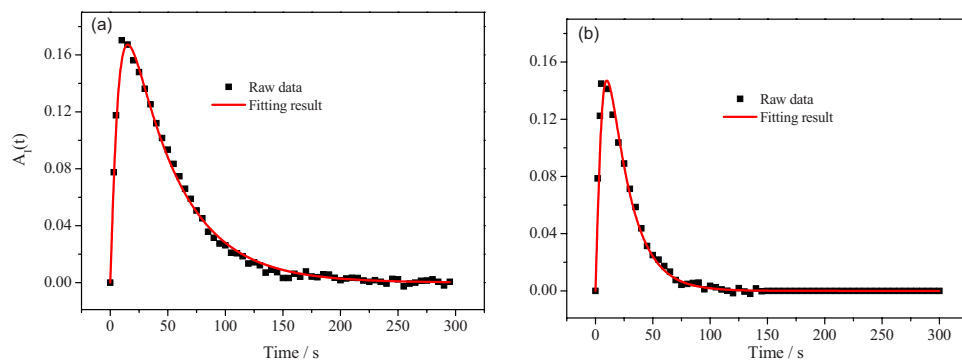


**Figure 5.** (Color online) IR raw data for  $(\text{CH}_3\text{OCH}_2^-)_{\text{ad}}$  (squares) and the fitting result (solid line) at (a) +300 and (b) +400 mV. See text for details.

than  $k_a$  except at 500 mV.  $k_b$  also increased with potential. A linear relation is found between 250 and 500 mV with a Tafel slope of  $220 \pm 20$  mV/dec. These results imply that the potential dependence of the initial dehydrogenation step ( $k_a$ ) is much lower than that of the CO formation step ( $k_b$ ). The reaction mechanism is discussed further in the next section.

**Discussion on reaction mechanism.**— The present study shows that the reaction activity of the DME dissociation is dependent on the electrode potential. We discuss these behaviors in the two potential regions: (i) Potential region I (50–100 mV) where the Pt electrode surface is covered with fully or highly adsorbed hydrogen and (ii) potential region II (100–500 mV) where the Pt electrode surface is covered with less or no hydrogen.

**Potential region between 50 and 100 mV.**— The rate constants of  $k_a$  and  $k_b$  were not directly calculated through the above analysis processes because reactions in the low potential region did not satisfy boundary conditions, which are necessary to solve the differential equations. It is clear from the electrochemical and in situ IR measurements that the formation of intermediates  $(\text{CH}_3\text{OCH}_2^-)_{\text{ad}}$  and product  $\text{CO}_{\text{ad}}$  are very slow when the electrode potential is lower than 100 mV (Fig. 2). The Pt electrode surface is highly or fully covered by hydrogen atoms in the potential region, indicating that the dehydrogenation process of DME is heavily retarded by

hydrogen adsorption. As the coverage of  $\text{H}_{\text{ad}}$  is higher than a certain value (for example, the coverage of  $\text{H}_{\text{ad}}$  on a Pt polycrystalline electrode surface is ca. 0.72 at 100 mV), the dehydrogenation process of DME is heavily prohibited. This implies that the dehydrogenation step of the DME molecule needs certain amounts of free Pt sites.

As previously reported by Tong et al.,<sup>8</sup> DME dissociation is completely inhibited on a cyanide covered Pt(111) surface. Because  $\text{CN}^-$  can form a stable adlayer of  $(2\sqrt{3} \times 2\sqrt{3})\text{R}30^\circ$  on a Pt(111) electrode surface,<sup>24</sup> it is proposed that the DME dissociation process needs at least three contiguous free Pt sites on the surface. We believe that a similar geometric effect is also present on the poly-Pt electrode surface and the high  $\text{H}_{\text{ad}}$  coverage at a negative potential region with fewer free Pt sites, which strongly retard the DME dissociation.

Furthermore, Kunimatsu et al.<sup>25</sup> reported that  $\text{H}_{\text{ad}}$  adsorbed at the terminal site of the polycrystalline Pt electrode surface is observed at a potential more negative than 100 mV during hydrogen evolution reactions. The terminal overpotential deposition  $\text{H}_{\text{ad}}$  may also retard the DME dissociation although direct evidence is not currently achieved. As the potential is higher than 100 mV,  $\text{H}_{\text{ad}}$  at the hollow sites (i.e., underpotential deposited  $\text{H}_{\text{ad}}$ ) on the Pt surface possibly provides more reaction space for the DME dissociation.

**Potential region between 100 and 500 mV.**— As shown in Fig. 6,  $k_a$  shows a very large Tafel slope ( $1200 \pm 100$  mV/dec) in the potential region between 150 and 400 mV. This behavior suggests that the reaction rate of the dehydrogenation step ( $k_a$ ) weakly depends on the electrode potential. This is because Pt surface atoms can selectively catalyze the C–H cleavage reaction in the dehydrogenation step of the DME dissociation process where potential has less of an effect. Thus, the DME dehydrogenation step on the Pt

**Table I.** DME dissociation rate constants ( $k_a$  and  $k_b$ ) obtained from the IR band at  $1322\text{ cm}^{-1}$  and  $\text{CO}_{\text{L}}$ .

Potential (mV)	$k_a$	$k_b$
150	$0.112 \pm 0.020$	$0.014 \pm 0.002$
200	$0.124 \pm 0.020$	$0.015 \pm 0.002$
250	$0.152 \pm 0.020$	$0.016 \pm 0.003$
300	$0.155 \pm 0.030$	$0.022 \pm 0.002$
350	$0.178 \pm 0.020$	$0.032 \pm 0.005$
400	$0.209 \pm 0.030$	$0.052 \pm 0.005$
450	$0.174 \pm 0.02$	$0.090 \pm 0.005$
500	$0.082 \pm 0.015$	$0.136 \pm 0.010$

**Table II.** DME dissociation rate constants ( $k_a$  and  $k_b$ ) obtained from the IR band at  $1480\text{ cm}^{-1}$  and  $\text{CO}_{\text{L}}$ .

Potential (mV)	$k_a$	$k_b$
150	$0.080 \pm 0.020$	$0.014 \pm 0.002$
200	$0.120 \pm 0.020$	$0.015 \pm 0.002$
250	$0.147 \pm 0.020$	$0.015 \pm 0.003$
300	$0.145 \pm 0.020$	$0.021 \pm 0.002$
350	$0.180 \pm 0.020$	$0.032 \pm 0.005$
400	$0.240 \pm 0.030$	$0.055 \pm 0.005$
450	$0.170 \pm 0.020$	$0.090 \pm 0.005$
500	$0.100 \pm 0.010$	$0.11 \pm 0.010$

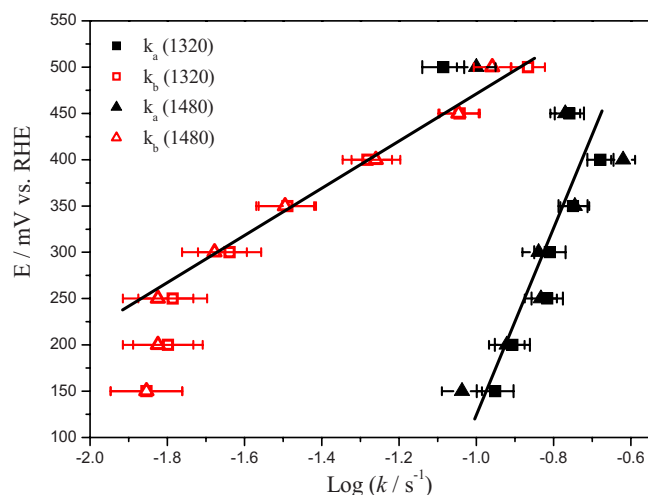
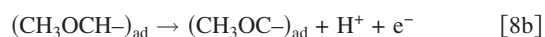


**Figure 6.** (Color online) Tafel plot of  $k_a$  and  $k_b$ . See text for details.

electrode surface can be regarded as a catalytic reaction rather than an electrocatalytic reaction. As the potential becomes higher than 450 mV, a competition reaction of anion adsorption is expected to show a large influence on the reaction activity, which can reduce the reaction rate at +500 mV (Fig. 6) or at a higher potential (results are not given).

In contrast to  $k_a$ ,  $k_b$  shows a smaller Tafel slope,  $220 \pm 20$  mV/dec (Fig. 6), indicating that the CO formation step in Eq. 1a strongly depends on the electrode potential compared to the dehydrogenation step and can be viewed as an electrocatalytic reaction. The following reaction scheme (Eq. 8) is considered as one of the possible mechanisms for CO formation in the potential region lower than 500 mV where  $\text{CO}_{\text{ad}}$  is stable upon further oxidation



The reaction intermediates of  $(\text{CH}_3\text{OCH}^-)_{\text{ad}}$ ,  $(\text{CH}_3\text{OC}^-)_{\text{ad}}$ , and  $\text{CH}_3\text{OH}_{\text{sol}}$  proposed in the scheme have not been observed in the present in situ IR measurement. A possible reason may be their relatively short lifetimes for these species due to the faster reaction rate of Eq. 8b and 8c than that of Eq. 8a. If one assumes that step 8a is the rate-determining step for the CO formation step, the Tafel slope is expected to be 120 mV/dec (assuming asymmetry parameter  $\alpha = 0.5$ ), which is still different from the present observation ( $220 \pm 20$  mV/dec).

On the present stage, although kinetics analysis based on the time-resolved IR measurement gives us useful information on the DME dissociation mechanism, it is still hard to make a final conclusion for its mechanism only from the Tafel slopes estimated above. Several problems are still present in the present analysis process. First, it was assumed in the present work that the IR band intensity of adsorbed CO species is linearly proportional to the CO coverage on the Pt electrode surface. This assumption is not exactly correct, especially for the surface covered by a high coverage where the strong dipole-dipole interaction between adsorbed CO molecules can greatly affect the IR absorption of CO.<sup>26,27</sup> Second, the coverage for CO adsorption on the Pt electrode surface is estimated only from  $\text{CO}_{\text{L}}$  for simplicity in the study. This is also not exactly correct because  $\text{CO}_{\text{B}}$  has been clearly observed from the IR measurements. Third, the simulation assumed that  $(\text{CH}_3\text{OCH}_3)_{\text{ad}}$ ,  $(\text{CH}_3\text{OCH}_2^-)_{\text{ad}}$ , and  $\text{CO}_{\text{ad}}$  occupy the same Pt surface sites during the decomposition process, which may not be very appropriate due to the different dimension and adsorption states. Better improvements in the fitting process are highly expected if these issues can be carefully treated.

### Conclusion

The kinetics of the electrocatalytic dissociation of DME on polycrystalline Pt electrode in an acidic solution has been quantitatively

analyzed by in situ IR spectroscopy. The present study indicates that DME dissociation takes place in a consecutive two-step reaction. The dissociation rate constants of the first dehydrogenation step ( $k_a$ ) and the second CO formation step ( $k_b$ ) are determined by fitting the time-resolved IR spectra in the potential region between 150 and 500 mV.

### Acknowledgment

This research was supported by a Grant-in-Aid for Scientific Research (B) (19350099) from MEXT and PRESTO, Japan Science and Technology (JST) Agency.

Hokkaido University assisted in meeting the publication costs of this article.

### References

1. J. T. Muller, P. M. Urban, W. F. Holderich, K. M. Colbow, J. Zhang, and D. P. Wilkinson, *J. Electrochem. Soc.*, **147**, 4058 (2000).
2. M. M. Mench, H. M. Chance, and C. Y. Wang, *J. Electrochem. Soc.*, **151**, A144 (2004).
3. M. H. Shao, J. Warren, N. S. Marinkovic, P. W. Faguy, and R. R. Adzic, *Electrochem. Commun.*, **7**, 459 (2005).
4. Y. Liu, M. Muraoka, S. Mitsushima, K.-I. Ota, and N. Kamiya, *Electrochim. Acta*, **52**, 5781 (2007).
5. T. A. Semelsberger, R. L. Borup, and H. L. Greene, *J. Power Sources*, **156**, 497 (2006).
6. I. Mizutani, Y. Liu, S. Mitsushima, K. I. Ota, and N. Kamiya, *J. Power Sources*, **156**, 183 (2006).
7. Y. Zhang, L. L. Lu, Y. J. Tong, M. Osawa, and S. Ye, *Electrochim. Acta*, **53**, 6093 (2008).
8. Y. Tong, L. Lu, Y. Zhang, Y. Gao, G. Yin, M. Osawa, and S. Ye, *J. Phys. Chem. C*, **111**, 18836 (2007).
9. L. Lu, G. Yin, Y. Tong, Y. Zhang, Y. Gao, M. Osawa, and S. Ye, *J. Electroanal. Chem.*, **619–620**, 143 (2008).
10. T. H. M. Housmans and M. T. M. Koper, *J. Phys. Chem. B*, **107**, 8557 (2003).
11. S. C. S. Lai, S. E. F. Kleyn, V. Rosca, and M. T. M. Koper, *J. Phys. Chem. C*, **112**, 19080 (2008).
12. E. Herrero, K. Franaszczuk, and A. Wieckowski, *J. Phys. Chem.*, **98**, 5074 (1994).
13. K. Franaszczuk, E. Herrero, P. Zelenay, A. Wieckowski, J. Wang, and R. I. Masel, *J. Phys. Chem.*, **96**, 8509 (1992).
14. P. Waszczuk, G. Q. Lu, A. Wieckowski, C. Lu, C. Rice, and R. I. Masel, *Electrochim. Acta*, **47**, 3637 (2002).
15. M. Osawa, *Bull. Chem. Soc. Jpn.*, **70**, 2861 (1997).
16. M. Osawa, in *Handbook of Vibrational Spectroscopy*, Vol. 1, J. M. Chalmers and P. R. Griffiths, Editors, pp. 785–799, John Wiley & Sons, Chichester (2002).
17. A. Miki, S. Ye, and M. Osawa, *Chem. Commun. (Cambridge)*, **2002**, 1500.
18. Y. X. Chen, A. Miki, S. Ye, H. Sakai, and M. Osawa, *J. Am. Chem. Soc.*, **125**, 3680 (2003).
19. S. Ye, T. Kondo, N. Hoshi, J. Inukai, S. Yoshimoto, M. Osawa, and K. Itaya, *Electrochemistry (Tokyo, Jpn.)*, **77**, 2 (2009).
20. S. Ye, T. Ichihara, and K. Uosaki, *J. Electrochem. Soc.*, **148**, C421 (2001).
21. P. W. Atkins, *Physical Chemistry*, 5th ed., Oxford University Press, Oxford (2006).
22. N. Kizhakevariam, I. Villegas, and M. J. Weaver, *Surf. Sci.*, **336**, 37 (1995).
23. G. A. Somorjai, *Introduction to Surface Chemistry and Catalysis*, John Wiley & Sons, New York (1994).
24. A. Cuesta, *J. Am. Chem. Soc.*, **128**, 13332 (2006).
25. K. Kunimatsu, T. Senzaki, G. Samjesk, M. Tsushima, and M. Osawa, *Electrochim. Acta*, **52**, 5715 (2007).
26. I. Villegas and M. J. Weaver, *J. Chem. Phys.*, **101**, 1648 (1994).
27. M. W. Severson, C. Stuhlmann, I. Villegas, and M. J. Weaver, *J. Chem. Phys.*, **103**, 9832 (1995).